Insensitive cation effect on single-atom Ni catalyst allows selective electrochemical conversion of captured CO2 in universal media

Jae Hyung Kim
  Seoul National University

Hyunsung Jang
  Seoul National University

Woong Choi
  Korea Institute of Science and Technology

Hyewon Yun
  Seoul National University

Eun Chong Lee
  Seoul National University

Dongjin Kim
  Korea Institute of Science and Technology

Ji Won Kim
  Clean Energy Research Center, Korea Institute of Science and Technology, Seoul 02792

Si Young Lee
  Seoul National University

Yun Jeong Hwang (✉ yjhwang1@snu.ac.kr)
 Seoul National University   https://orcid.org/0000-0002-0980-1758

Abstract

The direct electroconversion of captured CO2 is attracting attention as an alternative to the current energy-demanding CO2 separation processes. In conventional capturing media, the reaction inevitably takes place in the presence of bulky ammonium, leading to steric hindrance and low CO selectivity. Here, for the first time, we present a single atom Ni catalyst (Ni−N/C) exhibits superior activity for the electroconversion of captured CO2, without the need for additives. In a CO2-captured monoethanolamine-based electrolyte, Ni−N/C achieves a notably high CO selectivity of 64.9% at −50 mA cm−2 integrated with a membrane electrode assembly. We also propose that Ni−N/C demonstrates weak cation sensitivity to the CO2 reduction reaction, maintaining high CO production activity in various capturing solutions, while Ag shows a gradual decrease depending on the bulkiness of the amine. These trends provide insights into selective catalyst design for the electroconversion of captured CO2 in universal media.

Introduction

Severe climate changes caused by anthropogenic carbon emissions have steered a global consensus toward carbon neutrality.[1−3] Accordingly, the development of efficient carbon capture, utilization, and storage (CCUS) technology has been recognized as one of the most urgent technologies to sustainable societies.[4,5] CO_2 from exhaust gases can be selectively captured using a basic solvent to which CO_2 can be readily bound as carbamate or bicarbonate, and the captured CO_2 is separated either by thermal or pressure swings for utilization.[6,7] However, the regeneration processes are energy-intensive, imposing a huge penalty on the operating cost of the overall CCUS processes.[8,9] Moreover, during the high-temperature stripping operation, amine-based capturing media suffer from oxidative and thermal degradation.[10,11] To overcome these drawbacks, the direct utilization of captured CO_2, which omits the CO_2 separation step, has been evaluated to enhance the feasibility of CCUS.[12−15]

The direct electroconversion via the captured-CO_2 reduction reaction (cCO_2RR) has been proposed utilizing the CO_2 absorption media as the electrolyte (Fig. 1a).[16−27] However, inferior selectivity toward CO or formate has been exhibited compared with that of the conventional CO_2-fed electrochemical reduction reaction (CO_2RR).[28] The electrocatalytic activity is determined by the charge transfer at the electrode−electrolyte interface, which necessitates the thorough investigation of cCO_2RR in terms of the interactions with the absorbent medium to improve the conversion activity. Yet, it is still in the early stages of research, and the previous studies have focused either on the fundamental catalyst material itself or the electrolyzer configuration. The low CO production from electroreduction of the bicarbonate has recently been tackled by using a bipolar membranes (BPM) to develop a proton-rich environment in the vicinity of the cathode in a membrane electrode assembly. The acidified environment helps the chemical equilibrium shift in favor of CO_2 by the following reaction (Equation (1)):

$$CO_2 + H_2O \rightleftharpoons H_2CO_3 \rightleftharpoons H^+ + HCO_3^- \qquad (1)$$
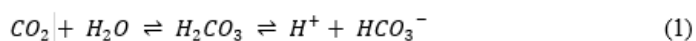
This increases the local CO_2 concentration near the cathode and promotes CO production. Such a strategy, however, has been demonstrated in the bicarbonate electrolyte.

The industrial-standard CO_2 capturing medium is a 30 wt.% monoethanolamine (MEA) aqueous solution that has a higher CO_2 absorption capacity and kinetics.[24] Unfortunately, the selective cCO_2RR has been more challenging in MEA-based electrolytes, in which CO_2 forms bulky ions, e.g.,

$$2HOC_2H_2NH_2 + CO_2 \rightleftharpoons HOC_2H_2NH_3^+ + HOC_2H_2NHCOO^- \qquad (2)$$
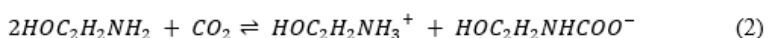
The bulky cations can construct an electric double layer (EDL) at the cathode surface, which hinders the cCO_2RR.[26,29] It has been proposed that alkali metal salts, which have a smaller effective cation radius and allow better access to captured CO_2 on the catalyst surface, are required to achieve the CO production in the cCO_2RR.[26] However, in pure amine-based absorbent media with no metal salt additives, poor CO production has still been observed (Supplementary Table 1) and further research is required to understand this activity. Furthermore, in the practical CO_2 capture process, a wide range of amine-based solvent formulations has been exploited to enhance the CO_2 absorption or regeneration rate.[30] Therefore, understanding universal performance in diverse capturing media is important in bringing the immediate applications of the cCO_2RR to industry.

To attain high CO selectivity in practical CO_2 capturing media, it is also necessary to find active electrode materials and investigate its interaction with the electrolyte. Thus far, only metal catalysts have been utilized for the cCO_2RR (Supplementary Table 1). In the last decade, single atom catalysts (SACs), where metal atoms are fully dispersed on supports, have been explosively studied and an unprecedented catalytic reactivity has been exhibited for various catalytic reactions.[31] Single atom Ni catalysts embedded in N-doped carbon (Ni−N/C) have shown particularly impressive CO_2RR activity and selectivity toward CO compared to metal catalysts in suppressing the hydrogen evolution reaction (HER).[32,33] Moreover, the dominant carbon matrix of Ni−N/C would manifest the differing potential of zero charge (PZC) with a metal electrode. Such differences can affect the formation of the EDL, which would be effective in modulating the electrode−electrolyte interface for improving the performance of the cCO_2RR. Nevertheless, SACs have never been examined for the cCO_2RR.

Here, we demonstrate that the low cation sensitivity of the Ni−N/C catalyst allows the selective cCO_2RR in universal CO_2-capturing media, even in the exclusive presence of bulky cations. In CO_2-captured MEA, the maximum CO faradaic efficiency (F. E.) of Ni−N/C (63.2%) is superior to that of commercial Ag nanoparticles (cAg, 30.1%), and the maximum CO partial current density (j_{CO}) of Ni−N/C (−3.5 mA cm^{-2}) is three times higher than that of cAg (−0.9 mA cm^{-2}) in the H-cell. In the zero-gap membrane electrode assembly configuration, the CO F. E. of Ni−N/C (64.9%) is 2.5 times higher than that of cAg (25.5%) at −50 mA cm^{-2}, which is the highest performance ever reported in CO_2-captured MEA solution without additives. We further report that Ni−N/C can maintain the CO F. E. at as much as 50%, even in bulkier amine solutions, in contrast to cAg, where the CO F. E. gradually falls to 0% with increasing amine bulkiness. Through a cation control experiment, we identify that the reactivity of Ni−N/C for the CO_2RR is less influenced by the size of the cation compared with that of cAg. We propose that a high surface charge density induced by the positive-shifted PZC of Ni−N/C allows for a marginal cation effect, which enables the maintenance of high CO selectivity in bulky amine-based electrolytes, in addition to the excellent suppression of HER of Ni-N/C. To the best of our knowledge, this is the first report of a catalytic approach relieving the cation effect, which permits the universal electroconversion of captured CO_2.

Results

Preparation and characterization of Ni−N/C. The Ni−N/C catalyst was prepared by the thermal conversion of zeolitic imidazolate framework (ZIF)-8, with some modifications to previous work.[34] ZIF-8 was synthesized through the self-assembly of Zn^{2+} and imidazolate with a particle size of ~100 nm (Supplementary Fig. 1); Zn was replaced with Ni by ion-exchange. The resulting light-green powder was then carbonized at 1000 °C to produce a final product, Ni−N/C. Scanning electron microscopy (SEM) and transmission electron microscopy (TEM) images of Ni−N/C displayed rather contracted morphologies compared to ZIF-8 after high-temperature treatment (Supplementary Fig. 2).[35] From high-angle annular dark-field scanning transmission electron microscopy (HAADF-STEM) images of Ni−N/C (Fig. 1b and Supplementary Figs. 2c and d), bright dots can be observed on the support, indicating the generation of atomically dispersed Ni sites embedded on the N-doped carbon matrix without any agglomerated metal particles (Supplementary Fig. 3). Extended X-ray absorption fine structure (EXAFS) analysis confirms the structural information seen in the microscopy images (Fig. 1c). The Ni K-edge k^3-weighted extended EXAFS spectrum of Ni foil shows a major scattering peak at ~2.0 Å at reduced distances, which describes the Ni−Ni bond of metallic Ni. The EXAFS spectrum of Ni−N/C exhibits a Ni−N scattering peak at ~1.5 Å at reduced distances without the presence of an Ni−Ni scattering peak, from which the isolation of Ni atoms bound to the N-doped carbon support can be concluded.

The Ni 2p X-ray photoelectron spectroscopy (XPS) of Ni−N/C shows a peak around 855 eV (Fig. 1d), corresponding to Ni(II) phthalocyanine (NiPc), and indicates the ionic character of Ni in Ni−N/C. X-ray absorption near edge structure (XANES) spectra of Ni−N/C and NiPc also show similar edge positions (Fig. 1e), confirming the similar oxidation state (Ni^{2+}). In addition, the pre- and post-edge peaks in XANES spectra display distorted Ni−N/C coordination environments. The peak labeled A is usually attributed to square-planar structures such as NiPc, absent in Ni−N/C.[32,36] The higher intensity of peak B compared to that of peak C in the XANES spectrum of Ni−N/C can be explained by the distortion of D_{4h} symmetry, owing to the displacement of the metal centre,[37] and is potentially induced by high-temperature pyrolysis.

Electrochemical cCO_2RR reactivity of catalysts. The catalytic properties of Ni−N/C and cAg for the cCO_2RR were investigated in a CO_2-absorbed 5 M MEA aqueous solution. The electrocatalytic conversion was performed in an H-cell after purging with Ar for 10 min to remove unabsorbed CO_2 in the MEA solution. Ni−N/C was found to exhibit superior performance compared to cAg both in the j_{CO} and product selectivity. Ni−N/C has a maximum j_{CO} of −3.5 mA cm^{-2}, three times larger than cAg (−0.9 mA cm^{-2}, Fig. 1f). Furthermore, it

shows a maximum CO F. E. (63.2%) of approximately double that of cAg (30.1%) with suppressed HER selectivity (Fig. 1g and Supplementary Fig. 4). Notably, the CO F. E. of Ni−N/C is the highest value ever reported for the cCO$_2$RR in CO$_2$-adsorbed pure MEA electrolyte without CO$_2$ flow (Supplementary Table 1). In addition, the on-set potential of Ni−N/C (−0.45 V vs. RHE) is lower than that of cAg (−0.60 V vs. RHE), which demonstrates the excellent catalytic activity of Ni−N/C for the cCO$_2$RR to CO.

To examine the effect of metal centers on SACs, a number of different metal-based SACs were prepared. Mn-, Fe-, Co-, and Cu-based SACs can be obtained by controlling metal precursors during the ion-exchange step (Supplementary Fig. 5). In contrast with Ni, other metal SACs show almost zero j_{CO} with high H$_2$ selectivity in the cCO$_2$RR (Supplementary Fig. 6). On N-doped carbon (N/C) prepared without ion-exchange, the HER only takes place in high overpotential regions. These results demonstrate that the Ni center plays a key role in the selective cCO$_2$RR to CO. The changes in the oxidation state and structure of Ni−N/C during the cCO$_2$RR were further investigated through an *in situ* XANES analysis. From the *in situ* XANES spectra, significant changes in the structure of Ni−N/C during the cCO$_2$RR were not observed (Supplementary Fig. 7), illustrating the catalytic importance of the distorted coordination structure of single atom Ni catalyst, which allows for excellent catalytic performance in the cCO$_2$RR without electrolyte-modulating additives.

Practical applicability test using a zero-gap membrane electrode assembly. To evaluate the practical applicability of the cCO$_2$RR in high current density, an electrochemical characterization was additionally performed with a zero-gap membrane electrode assembly for the cCO$_2$RR in CO$_2$-captured 5 M MEA. BPM was used to drive the regeneration reaction of carbamate (RNHCOO$^-$ + H$^+$ → RNH$_2$ + CO$_2$), to increase the local concentration of CO$_2$ near the cathode and thus enhance conversion activity (Fig. 2a). At −50 mA cm^{-2}, the CO F. E. of Ni−N/C was 64.9% (Fig. 2b and Supplementary Fig. 8), which is approximately 2.5 times higher than that of cAg (25.5%), showing a similar trend to H-cell experiments and demonstrating the superior catalytic performance of Ni−N/C for the cCO$_2$RR in high current density. When an anion exchange membrane (AEM), the alkaline properties of which favor gas-fed CO$_2$ reduction reaction, is used, significantly lowered cCO$_2$RR selectivity has been observed for both Ni−N/C and cAg (Fig. 2b and Supplementary Fig. 8). This could be because AEM is inferior to proton transfer toward the cathode side. From these results, we propose that building a high concentration of liberated CO$_2$ is essential for the cCO$_2$RR at high current density of membrane electrode assembly, consistent with previous reports in bicarbonate solutions.[18] The activity difference in the usage of BPM with AEM provides information on the initial stage of the reaction pathway of cCO$_2$RR, which will be discussed in the following section.

The cCO$_2$RR was then performed in 5 M MEA using Ni−N/C in the membrane electrode assembly with chronopotentiometry at −50 mA cm^{-2} for 10 h. Since the reaction was carried out under Ar, the chemical equilibrium of adsorption/desorption of CO$_2$ in MEA (Equation (2)) continuously moves to favor desorption of CO$_2$. Hence, the number of carbamate anions and the desorption rate of CO$_2$ were gradually decreased over time, which caused a progressive drop in the CO F. E. after 10 h (Supplementary Fig. 9). Nevertheless, after the MEA solution was refreshed by CO$_2$ adsorption, the CO F. E. was recovered to ~50% under Ar conditions. This result demonstrates stable Ni−N/C catalyst operation for the cCO$_2$RR, and the reduction in CO selectivity is caused by the diminished amount of adsorbed CO$_2$ in the capturing medium. An important point to note here is the stability of the capturing media. To identify electrochemical degradation or modification of MEA, analysis of the MEA solution before and after the stability test was carried out by ^{1}H nuclear magnetic resonance (NMR) spectroscopy (Supplementary Fig. 10).[38] No additional ^{1}H NMR peaks were observed after the stability test, indicating the stable operation of MEA during the cCO$_2$RR without electrochemical modifications. This result demonstrates that the cCO$_2$RR is a promising catalytic system that could even resolve the degradation problems of capturing media in conventional CCUS processes.

Reaction pathway of the cCO$_2$RR. Next, we designed experiments to understand the pathways of the cCO$_2$RR and investigate the effects of different catalysts. First, two scenarios can be considered at the initial stage: i) the active site of the catalyst directly attacks the carbamate anion, or ii) CO$_2$ is released from the MEA followed by electrocatalytic conversion by similar pathways to conventional CO$_2$RR (Fig. 3a). A combination of these two scenarios is also possible. Sargent et al. argued for the direct reduction of the MEA−CO$_2$ adduct (carbamate) through the detection of the ethanolammonium cation on the electrode surface using *in situ* surface-enhanced Raman spectroscopy,[26] whereas Goetheer et al. considered the liberated CO$_2$ to be the reactant in temperature-controlled experiments.[27] In conventional CO$_2$RR-to-CO, the reaction is initiated by electron injection into CO$_2$, resulting in the unstable CO$_2^-$ intermediate, which is typically regarded as the rate-determining step (RDS).[39,40] The stabilization of this intermediate on the catalyst surface is the key to facilitating the CO$_2$RR. In the cCO$_2$RR, if the direct reduction of carbamate takes place in the initial stage of the reaction as in scenario (i) and the electron transfer step to carbamate is the RDS of the reaction, the CO production reaction rate with respect to carbamate

concentration could help identify the initial stage. Thus, in CO_2-absorbed 1−5 M MEA solutions, the electrochemical conversion rate of captured CO_2 was measured with both Ni−N/C and cAg. The carbamate concentration of the respective MEA solution was determined by quantitative analysis of NMR data (Supplementary Fig. 11) using internal standards. The j_{CO} for both catalysts is not significantly affected by the concentration of carbamate (Supplementary Fig. 12). Hence, the reaction is considered zeroth-order with respect to carbamate (Fig. 3b), i.e., the reaction rate is independent of the concentration of carbamate for both catalysts. From these results, we speculated that the reactant was in fact the released CO_2 from carbamate rather than the carbamate itself.

To regulate the amount of CO_2 released in the H-cell, the reaction temperature was controlled. Since the regeneration reaction is endothermic,[41] the rate of the reaction can be accelerated by increasing the reaction temperature. As the reaction temperature is increased from 5 °C to 40 °C, the limiting current density ($j_{lim.}$) increases for both catalysts (Ni−N/C: -0.52 mA cm^{-2} (5 °C) → −1.85 mA cm^{-2} (RT) → −3.5 mA cm^{-2} (40 °C); cAg: 0 (5 °C) → −0.39 mA cm^{-2} (RT) → −0.91 mA cm^{-2} (40 °C), Figs. 3c and d). If the direct reduction of carbamate occurs in the cCO$_2$RR, the mass transport limit in such low current density is difficult to detect. Furthermore, the amount of carbamate in the electrolyte is reduced as the reaction temperature is increased, and thus even if the $j_{lim.}$ originates from the mass diffusion of carbamate, the $j_{lim.}$ has to be decreased. On the other hand, the increased amount of liberated CO_2 can improve $j_{lim.}$, solidifying the proposition of liberated CO_2 being the reactant. The sharp increase in reaction rate by the BPM being used in the membrane electrode assembly experiment is consistent with this scenario. It should be noted that the decrease in $j_{lim.}$ at 60 °C may originate from the drop in CO selectivity due to H_2 being rapidly generated at high temperatures (Supplementary Fig. 13). Therefore, for the effective electrochemical conversion of captured CO_2, the optimal temperature should be found, which involves the trade-off between the amount of liberated CO_2 and the reaction rate of HER.

From the experimental results discussed, it can be concluded that the superior performance of Ni−N/C cannot be attributed to the different initial reactions of cAg and Ni−N/C for the cCO$_2$RR. The cCO$_2$RR pathway appears to be comparable to the conventional CO_2RR, but with a reduced concentration of CO_2 in the cCO$_2$RR. Thus, the high performance of Ni−N/C must originate from the high tolerance of low CO_2 concentrations in the CO_2RR because of its superior CO_2RR intrinsic activity and high activation energy for the HER, as we previously reported with low-concentration CO_2 gas experiments.[33]

Universal reactivity of Ni−N/C for the cCO$_2$RR. Subsequently, we investigate how Ni−N/C exhibits high reactivity in the presence of bulky ammonium cations for the cCO$_2$RR. In order to stabilize the CO_2^- intermediate in the CO_2RR, cations with high surface charge density on the cathode are essential.[29] Thus, a smaller effective size of alkali metal cation, which creates a higher surface charge density on the cathode, is beneficial to the performance of the CO_2RR.[42−47] However, amine-based capturing media inevitably generate bulky ammonium cations in the adsorption of CO_2, which hampers the stabilization of the CO_2^- intermediate. However, the effect of bulky cations in the cCO$_2$RR has not yet been investigated. To understand the effects of bulky cations, we carried out the cCO$_2$RR in systems wherein the bulkiness of the capturing molecule can be controlled. The electrocatalytic performances were examined in six different CO_2 capturing media (1 M of potassium bicarbonate, MEA, 3-amino-1-propanol, 2-(methylamino)ethanol, 2-amino-2-methyl-1-propanol, and diethanolamine), (Figs. 4a−4f and Supplementary Fig. 14). The effect of the properties of absorbents on activity trends is also discussed below, with the aim of gaining insights into the activity for the cCO$_2$RR (Figs. 4g and h).

Both j_{CO} and CO F. E. were found to decrease with increasing bulkiness of capturing media for both Ni−N/C and cAg. One noticeable difference between Ni−N/C and cAg was activity sensitivity depending on cation type. The bulkiness of the cation has a significant impact on cAg, showing a dramatic loss in j_{CO} as the effective size of the cation increases. The j_{CO} of cAg fell as low as zero in diethanolamine, a secondary amine (Fig. 4h). In contrast, the j_{CO} of Ni−N/C is less affected by the effective cation size (Fig. 4g), and the CO F. E. of Ni−N/C was maintained at ~ 50%, irrespective of the electrolyte type (Figs. 4a−4f). From these results, we hypothesized that the marginal cation effect is manifested on Ni−N/C, and the weak cation sensitivity allows the selective cCO$_2$RR in universal absorbent media. We note, however, that the different types of amine electrolytes not only change the size of the cation but also alter the amount of desorbed CO_2 and viscosity of the solvent, which can render the decoupling of the cation effect difficult.

Weak cation sensitivity of Ni−N/C for the CO_2RR. To exclusively identify the difference in cation sensitivity of catalysts, we measured the activity and selectivity of the CO_2RR in CO_2-saturated 0.05 M carbonate electrolytes containing different alkali metal cations (Li$^+$, Na$^+$, K$^+$, and Cs$^+$). Similar to the amine solutions, the j_{CO} of Ni−N/C and cAg decreased as the effective cation radius increased from

Cs$^+$ to Li$^+$ (Figs. 5a and b), but the cation sensitivity was clearly different in Ni−N/C compared to cAg. The maximum CO F. E. of Ni−N/C (~100 %) was maintained irrespective of the electrolyte used, whereas that of cAg was reduced to ~85 % in 0.05 M Na$_2$CO$_3$ and ~75 % in 0.05 M Li$_2$CO$_3$ (Figs. 5c and d). The normalized j_{CO} by j_{CO} in the presence of Cs$^+$ is higher in Ni−N/C than that in cAg, and the slope of the normalized value with respect to the effective cation radius of Ni−N/C is less steep than that of cAg (Fig. 5e). These results demonstrate that the cation sensitivity can be varied depending on the type of catalyst and that Ni−N/C shows weaker cation sensitivity compared with cAg.

The accumulated cation density at the EDL can be determined by the size of the cation, the applied potential, and the PZC of the electrode.[48] The weak cation sensitivity of Ni−N/C may arise from its relatively high PZC. In the presence of any cation, Ni−N/C exhibits a ~0.6 V higher PZC compared to cAg (Supplementary Fig. 15). This positive-shifted PZC can create an increased surface charge density for the same applied potential in the reduction reaction, which in turn may be prone to stabilizing the CO$_2^-$ intermediate, thus mitigating the cation effect. The positive-shifted PZC of Ni−N/C, therefore, allows for the effective accumulation of cations to stabilize the CO$_2^-$ intermediate, even in the presence of large cations such as Li$^+$ or ammonium, without additives. The marginal cation effect on Ni−N/C permits the selective cCO$_2$RR in universal capturing media.

Conclusions

We have demonstrated that Ni−N/C is an effective catalyst for the direct electroconversion of captured CO$_2$ by amine-based absorbents. Ni−N/C showed 64.9 % of maximum CO F. E. at −50 mA cm^{-2} for the cCO$_2$RR, making it the highest value ever reported in CO$_2$-captured MEA solution without CO$_2$ flow and additives. To understand the initial stage of the reaction in the capture media, the CO productivity was investigated by controlling the carbamate concentration, reaction temperature, and type of membrane in the membrane electrode assembly, which provided evidence for liberated CO$_2$ being the reactant in the cCO$_2$RR. We have also proposed that Ni−N/C is a universal catalyst to maintain high CO selectivity in various amine-based absorbent for the cCO$_2$RR. By controlling the size of cations in carbonate electrolytes, we further demonstrate that the CO$_2$RR performance of Ni−N/C is less affected by cation size compared to that of cAg. The weak cation sensitivity allows for the maintenance of a CO F. E of Ni−N/C of up to 50%, even in bulkier capturing media. This distinguishes it from commercial Ag, where it was found that the CO F.E. gradually decreased to 0% with increasing amine bulkiness. In addition to high suppressing ability of HER, the weak cation effect of Ni−N/C may be attributed to the high PZC of Ni−N/C, which can maintain a high surface charge density, irrespective of the size and bulkiness of cations. We envisage that these results will provide important catalytic insights into integrated CO$_2$ capture and electroconversion systems and the preparation of catalysts for them.

Methods

Chemicals. Zinc nitrate hexahydrate (Zn(NO$_3$)$_2$·6H$_2$O, ≥99.0%), 2-methylimdazole (MeIM, 99%), manganese nitrate hydrate (Mn(NO$_3$)$_2$·xH$_2$O, 99.99%), iron chloride (FeCl$_2$, 98%), copper nitrate trihydrate (Cu(NO$_3$)$_2$·3H$_2$O, 99-104%), 5 wt.% Nafion, ethanolamine (≥99.0%), diethanolamine (≥99.0%), potassium bicarbonate (≥99.7%), 3-amino-1-propanol (99%), 2-(methylamino)ethanol (≥98%), and 2-amino-2-methyl-1-propanol (≥95%) were purchased from Sigma−Aldrich. Methanol (99.5%), n-hexane (95%), ethanol (94.5%) and 2-propanol (99.8%) were purchased from Samchun Chemicals (Korea). Nickel nitrate hexahydrate (Ni(NO$_3$)$_2$·6H$_2$O, crystalline/certified) was purchased from Fisher Chemicals. Cobalt nitrate hexahydrate (Co(NO$_3$)·6H$_2$O, 99-102%), carbon paper (TGP-H-120 20%WP, Toray), commercial Ag (20-40 nm, 99.9%), and IrO$_2$ (Premion®, 99.99%) were purchased from Alfa Aesar. AEM (Sustanion X37-50 Grade RT) for the membrane electrode assembly was purchased by Dioxide Materials. BPM (Fumasep FBM-PK, FuMA-Tech), PtTi mesh, and gas diffusion layers (GDL, Sigracet 39 BB, SGL Carbon) were purchased from Fuel Cell Store. All chemicals were utilized without further purification.

Synthesis of ZIF-8. ZIF-8 was synthesized by a previously-reported method, with some modifications.[32] After Zn(NO$_3$)·6H$_2$O (2.93 g) and MeIM (6.49 g) were each separately dissolved completely in methanol (100 mL), the solutions were mixed by magnetic stirring at room temperature (RT) for 24 h to induce the self-assembly between metal nodes and organic linkers. The resulting suspension was vacuum-filtered and washed several times with methanol. The resulting white powder was then dried overnight at 80 °C.

Synthesis of ZIF-8-derived M−N/C catalysts. To produce ZIF-8-derived single atom Ni−N/C catalysts, Zn was replaced by Ni in an ion-exchange reaction. Prior to the ion-exchange, ZIF-8 (0.100 g) was dispersed in hexane (10 mL) by sonication for 15 min.

$Ni(NO_3)\cdot 6H_2O$ solution (0.6 M, 25 µL) was added dropwise to the ZIF-8-dispersed hexane suspension under sonication. The ion-exchange reaction was carried out under vigorous stirring (1000 rpm) at RT for 3 h. The ion-exchanged ZIF-8 was separated from hexane by centrifugation (8000 rpm for 10 min). The resulting powder was dried overnight at 80 °C. The dried powder was carbonized at 1000 °C at a ramping rate of 4.9 °C min^{-1} for 2 h under Ar flow. To prepare single atom Mn, Fe, Co, or Cu catalysts, $Ni(NO_3)\cdot 6H_2O$ is replaced by $Mn(NO_3)_2\cdot xH_2O$, $FeCl_2$, $Co(NO_3)_2\cdot 6H_2O$, and $Cu(NO_3)_2\cdot 3H_2O$, respectively, in the ion-exchange step.

Material characterizations. SEM images were captured using an Inspect F instrument (FEI). The TEM, HAADF-STEM, and energy dispersive spectroscopy images were obtained by TECNAI F20 G^2 (FEI), Titan 80-300 (FEI) equipped with a double-sided spherical aberration (Cs) corrector, and Talos F200X (FEI), respectively. XPS spectra were obtained using a Nexsa (Thermo Fisher Scientific) with a monochromated Al-Kα source. The X-ray absorption fine structure (XAFS) was analyzed at the 1D KIST−PAL beamline of the Pohang Light Source (PLS-II) in a 3.0 GeV storage ring with a ring current of 250 mA. The X-ray beam was monochromated by a Si(111) double crystal. The XAFS spectra were collected in transmission and fluorescence modes. An electrochemical *in situ* XAFS analysis was performed using the modified H-cell. The catalyst-loaded (1 mg cm^{-1}) carbon paper strip was attached to the window of the H-cell and sealed with Kapton tape. An Ag/AgCl (3 M KCl filling solution) reference electrode and Pt plate counter electrode were used to form the three-electrode system. The XAFS spectra were obtained in CO_2-adsorbed MEA (5 M) solution after applying a fixed potential for 10 min from the fluorescence mode with Ar gas purging. The post-treatment of the obtained spectra was performed by Demeter software.

Electrochemical characterizations. Electrochemical characterizations were performed using an IviumStat electrochemical analyzer in a gas-tight H-cell using a three-electrode system. To prepare the working electrodes, catalysts were deposited onto carbon paper (area: 0.5 cm^2) using 500 µL of catalaminyst ink spray. The catalyst ink was prepared by dispersing catalysts (3 mg) in a mixture of 2-propanol (3 mL) and 5 wt.% Nafion solution (30 µL) under sonication for 30 min. Ag/AgCl and Pt plate electrodes were used for the reference and counter electrodes, respectively. To separate the catholyte and anolyte, an AEM (Selemion AMV) was used. $KHCO_3$ (0.5 M) was used as an anolyte. As catholytes, Ar (99.999%)-saturated monoethanolamine (1−5 M), $KHCO_3$ (1 M), 3-amino-1-propanol (1 M), 2-(methylamino)ethanol (1 M), 2-amino-2-methyl-1-propanol (1 M), and diethanolamine (1 M) were used after CO_2-adsorption by CO_2 (99.99%) flow for at least 1 h. The activity and selectivity of catalysts for the CO_2RR were measured by chronoamperometry, by applying fixed potentials under Ar flow, at a flow rate of 100 sccm. Prior to applying each potential, CO_2-capture and Ar-saturation steps were sequentially carried out for 10 min each. *iR*-compensation was conducted for each potential by determining a series resistance from electrochemical impedance spectroscopy (EIS). Potential conversion into the reversible hydrogen electrode (RHE) scale was performed using Equation (3):

$$E(vs. RHE) = E(vs. Ag/AgCl) + 0.210\,V + 0.059\,V \times pH \qquad (3)$$

All electrochemical characterizations were carried out in a water bath set to 40 °C, except in temperature-controlled experiments. Cation sensitivity was investigated in CO_2-saturated 0.05 M M_2CO_3 electrolytes (M: Li, Na, K, and Cs) at RT. Differential capacitance was measured to obtain the PZC of catalysts in 0.05 M M_2CO_3 electrolyte with a frequency of 100 mHz and a 10 mV potential amplitude. The capacitance, C, was calculated by Equation (4),

$$C = -(\omega Z_{Im})^{-1} \qquad (4)$$

where ω denotes the frequency and Z_{Im} denotes the imaginary part of the Nyquist plot of EIS.

Membrane electrode assembly electrolyzer experiment. The practicability test of the direct electrochemical conversion of captured-CO_2 was performed using a custom-designed membrane electrode assembly electrolyzer with a zero-gap configuration (Supplementary Fig. 16). The anode was prepared by spraying 1.2 mL of IrO_2 ink on quadruply stacked sheets of PtTi mesh. The IrO_2 ink was prepared by dispersing IrO_2 (0.300 g) in a mixture of 2-propanol (10 mL) and 5 wt.% Nafion solution (1.2 mL) under sonication for 30 min. The cathode was assembled by spraying a catalyst ink on a GDL (area: 5 cm^2). The catalyst ink was prepared by mixing catalyst (9 mg), 2-propanol (1.5 mL), and 5 wt.% Nafion solution (90 µL) under sonication for 30 min. The cathode catalyst layer, membrane, and anode were stacked with a zero-gap. For the membrane, either BPM or AEM were applied. $KHCO_3$ (0.5 M) and MEA (5 M) aqueous electrolytes were used as the anolyte and catholyte, respectively. The electrolytes were circulated around a flow channel of bipolar plates using a peristaltic pump at a rotating speed of 16 rpm. The catalytic properties were evaluated by chronopotentiometry under Ar flow at a flow

rate of 100 sccm, after the CO_2-capture and Ar-saturation steps were sequentially carried out over 10 min. The temperature of the membrane electrode assembly electrolyzer was set to 40 °C by temperature controllers connected to the bipolar plates.

Gaseous product analysis. The gaseous products were quantified at fixed potentials or currents using gas chromatography (GC, Agilent 7890B). The gas flow outlet in the H-cell or the membrane electrode assembly electrolyzer was directly connected to the GC inlet. The gaseous products were injected using a six-port valve system. Ar (99.999%) was used as the carrier gas, and a Carboxen 1000 packed column (Supelco) was used. The number of gaseous products was quantified using a thermal conductivity detector or a flame ionization detector equipped with a methanizer depending on the concentration of CO. The F.E. of gaseous products was calculated by Equation (5):

$$F.E._{H_2 \, or \, CO} = i_{H_2 \, or \, CO} \, / \, (i_{H_2} + i_{CO}) \times 100 \qquad (5)$$

where i_{H_2} and i_{CO} indicate partial current of H_2 and CO, respectively. The $i_{H_2 \, or \, CO}$ was obtained using Equation (6):

$$i_{H_2 \, or \, CO} = C_{H_2 \, or \, CO} \times Q \times \frac{2FP_0}{RT} \qquad (6)$$

where $C_{H_2 \, or \, CO}$, Q, F, P_0, R, and T indicate the volume concentration of H_2 or CO, flow rate of gas, atmospheric pressure, ideal gas constant, and temperature, respectively.

Quantitative analysis of ^{1}H NMR. The concentration of carbamate was quantified by ^{1}H NMR (Varian 500, Agilent). To prepare a solution for NMR measurement, the MEA solutions (1−5 M) were diluted by mixing 5 µL of MEA solution with 495 µL of deionized water. Subsequently, 450 µL of the diluted solutions was added to 50 µL of D_2O in which 50 mmol of dimethyl sulfoxide (DMSO) was dissolved. The concentration of carbamate was determined by comparison with the integrated peak area between the carbamate and the DMSO internal standard.

Estimation of effective cation radius. The effective cation radius was estimated with reference to previous reports.[29,49,50] The effective cation radii of CO_2-adsorbed MEA, 3-amino-1-propanol, 2-amino-2-methyl-1-propanol, and diethanolamine were estimated from the reported effective cation radii of ethylammonium, isopropylammonium, isobutylammonium, diethylammonium, respectively. The effective cation radius of CO_2-adsorbed 2-(methylamino)ethanol was estimated by halving the sum of the effective cation radii of dimethylammonium and diethylammonium.[49] The effective cation radius of K^+ was estimated by considering the relative effective radius between ethyl ammonium and K^+ in the previous report.[50] The effective cation radius of other alkali metal cations (Li^+, Na^+, and Cs^+) was estimated using the relative effective radius between K^+ and M^+ in the previous report.[29]

References

1. Voosen, P. *Science* **373**, 474−475. (2021).
2. *IPCC Sixth Assessment Report* (Intergovernmental Panel on Climate Change, 2021).
3. *The Paris Agreement* (United Nations, 2015).
4. *CCUS in Clean Energy Transition* (International Energy Agency, 2020)
5. Bui. M. et al. Carbon capture and storage (CCS): the way forward. *Energy Environ. Sci.* **11**, 1062−1176 (2018).
6. Rochelle, G. T. Amine scrubbing for CO_2 capture. *Science* **325**, 1652−1654 (2009).
7. Keith, D. W., Holmes, G., Angelo, D. St. & Heidel, K. A process for capturing CO_2 from the atmosphere. *Joule* **2**, 1573−1594 (2018).
8. Gao, W. et al. Industrial carbon dioxide capture and utilization: state of the art and future challenges. *Energy Environ. Sci.* **49**, 8584−8686 (2020).
9. Kar, S., Goeppert, A. & Prakash, S. K. S. Integrated CO_2 capture and conversion to formate and methanol: connecting two threads. *Acc. Chem. Res.* **52**, 2892−2903 (2019).
10. Chi, S. & Rochelle, G. T. Oxidative degradation of monoethanolamine. *Int. Eng. Chem. Res.* **41**, 4178−4186 (2002).
11. J. Davis & Rochelle, G. Thermal degradation of monoethanolamine at stripper conditions. *Energy Procedia* **1**, 327−333 (2009).

12. Renfrew, S. E., Starr, D. E., Strasser, P. Electrochemical approaches toward CO_2 capture and concentration. *ACS Catal.* **10**, 13058–13074 (2020).

13. Zhang, S., Chen, C., Li, K., Yu, H. & Li, F. Materials and system design for direct electrochemical CO_2 conversion in capture media. *J. Mater. Chem. A* **9**, 18785–18792 (2021).

14. Sullivan, I. et al. Coupling electrochemical CO_2 conversion with CO_2 capture. *Nat. Catal.* **4**, 952–958 (2021).

15. Gallant, B. M. *Nat. Energy* **6**, 13–14 (2021).

16. Hori, X. & Suzuki, S. Electrolytic reduction of bicarbonate ion at a mercury electrode. *J. Electrochem. Soc.* **130**, 2387–2390 (1983).

17. Min, X. & Kanan, M. W. Pd-catalyzed electrohydrogenation of carbon dioxide to formate: high mass activity at low overpotential and identification of the deactivation pathway. *J. Am. Chem. Soc.* **137**, 4701–4708 (2015).

18. Li, T. et al. Electrolytic conversion of bicarbonate into CO in a flow cell. *Joule* **3**, 1487–1497 (2019).

19. Li, Y. C. *et al.* CO_2 electroreduction from carbonate. *ACS Energy Lett.* **4**, 1427–1431. (2019).

20. Lees, E. W. et al. Electrodes designed for converting bicarbonate into CO. *ACS Energy Lett.* **5**, 2165–2173 (2020).

21. Li, T., Lees, E. W., Zhang, Z. & Berlinguette, C. P. Conversion of bicarbonate to formate in an electrochemical flow reactor. *ACS Energy Lett.* **5**, 2624–2630 (2020).

22. Fink, A. G. et al. Impact of alkali cation identity on the conversion of HCO_3^- to CO in bicarbonate electrolyzers. *ChemElectroChem* **8**, 2094–2100 (2021).

23. Zhang, Z. et al. Porous metal electrodes enable efficient electrolysis of carbon capture solutions. *Energy Environ. Sci.* https://doi.org/10.1039/D1EE02608A (2022).

24. Chen, L. et al. Electrochemical reduction of carbon dioxide in a monoethanolamine capture medium. *ChemSusChem* **10**, 4109–4118 (2017).

25. Abdinejad, M., Mirza, Z., Zhang, X.-A. & Kraatz, H.-B. Enhanced electrocatalytic activity of primary amines for CO_2 reduction using copper electrodes in aqueous solution. *ACS Sustainable Chem. Eng.* **8**, 1715–1720 (2020).

26. Lee, G. et al. Electrochemical upgrade of CO_2 from amine capture solution. *Nat. Energy* **6**, 46–53 (2021).

27. Pérez-Gallent, E. Vankani, C., Sánchez-Martínez, C., Anastasopol, A. & Goetheer, E. Integrating CO_2 capture with electrochemical conversion using amine-based capture solvents as electrolytes. *Ind. Eng. Chem. Res.* **60**, 4269–4278 (2021).

28. Salvatore, D. A. et al. Designing anion exchange membranes for CO_2 electrolysers. *Nat. Energy* **6**, 339–348 (2021).

29. Ringe, S. et al. Understanding cation effects in electrochemical CO_2 reduction. *Energy Environ. Sci.* **12**, 3001–3014 (2019).

30. Vega, F. et al. Carbon dioxide chemistry, capture and oil recovery Ch. 8 (IntechOpen, 2018).

31. Mitchell, S. & Pérez-Ramírez, J. Single atom catalysis: a decade of stunning progress and the promise for a bright future. *Nat. Commun.* **11**, 4302 (2020).

32. Sa, Y. J. et al. Thermal transformation of molecular $Ni^{2+}-N_4$ sites for enhanced CO_2 electroreduction activity. *ACS Catal.* **10**, 10920–10931 (2020).

33. D. Kim et al. Electrocatalytic reduction of low concentrations of CO_2 gas in a membrane electrode assembly electrolyzer. *ACS Energy Lett.* **6**, 3488–3495 (2021).

34. Zhao, C. et al. Ionic exchange of metal-organic frameworks to access single nickel sites for efficient electroreduction of CO_2. *J. Am. Chem. Soc.* **139**, 8078–8081 (2017).

35. Wei, S. et al. Direct observation of noble metal nanoparticles transforming to thermally stable single atoms. *Nat. Nanotechnol.* **13**, 856–861 (2018).

36. Gaur, A. et al. XAFS study of copper(II) complexes with square planar and square pyramidal coordination geometries. *J. Mol. Struct.* **1118**, 212–218 (2016).

37. Jia, Q. et al. Experimental observation of redox-induced Fe–N switching behavior as a determinant role for oxygen reduction activity. *ACS Nano* **9**, 12496–12505 (2015).

38. Perinu, C. Arstad, B. Jens, K.-J. NMR spectroscopy applied to amine–CO_2–H_2O systems relevant for post-combustion CO_2 capture: A review. *Int. J. Greenh. Gas Con.* **20**, 230–243 (2014).

39. Cheng, T. Xiao, H. Goddard III, W. A. Reaction mechanisms for the electrochemical reduction of CO_2 to CO and formate on the Cu(100) surface at 298 K from quantum mechanics free energy calculations with explicit water. *J. Am. Chem. Soc.* **138**, 13802–13805 (2016).

40. Singh, M. R. Goodpaster, J. D. Weber, A. Z. Head-Gordon, M. Bell, A. T. Mechanistic insights into electrochemical reduction of CO_2 over Ag using density functional theory and transport models. *Proc. Natl. Acad. Sci. U. S. A.* **114**, E8812–E8821 (2017).

41. Song, C. Kansha, Y. Ishizuka, M. Fu, Q. Tsutsumi, A. Design of low-cost CO_2 capture process based on heat integration technology. *Energy Procedia* **61**, 365–368 (2014).

42. Strmcnik, D. et al. The role of non-covalent interactions in electrocatalytic fuel-cell reactions on platinum. *Nat. Chem.* **1**, 466–472 (2009).

43. Singh, M. R., Kwon, Y., Lum, Y., Ager, J. W. & Bell, A. T. Hydrolysis of electrolyte cations enhances the electrochemical reduction of CO_2 over Ag and Cu. *J. Am. Chem. Soc.* **138**, 13006–13012 (2016).

44. Chen, L. D., Urushihara, M., Chan, K. & Nørskov, J. K. Electric field effects in electrochemical CO_2 reduction. *ACS Catal.* **6**, 7133–7139 (2016).

45. Resasco, J. et al. Promoter effects of alkali metal cations on the electrochemical reduction of carbon dioxide. *J. Am. Chem. Soc.* **139**, 11277–11287 (2017).

46. Hussain, G. et al. How cations determine the interfacial potential profile: relevance for the CO_2 reduction reaction. *Electrochim. Acta* **327**, 135055 (2019).

47. Monteiro, M. C. O. et al. Absence of CO_2 electroreduction on copper, gold and silver electrodes without metal cations in solution. *Nat. Catal.* **4**,654–662 (2021).

48. Shin, S.-J. et al. On the importance of the electric double layer structure in aqueous electrocatalysis. *Nat. Commun.* **13**, 174 (2022).

49. Becker, M., Kluner, T. & Wark, M. Formation of hybrid ABX_3 perovskite compounds for solar cell application: first-rpinciples calculations of effective ionic radii and determination of tolerance factors. *Dalton Trans.* **46**, 3500–3509 (2017).

50. Kour, R. et al. Potential substitutes for replacement of lead in perovskite solar cells: a review. *Global Challenges* **3**, 1900050 (2019).

Declarations

Acknowledgements

Author contributions

Y.J.H. supervised the project. Y.J.H. and J.H.K. conceived and designed the experiments and co-wrote the manuscript. J.H.K. conducted synthesis, physicochemical characterisation, and electrochemical analysis with assistance from H.J., W.C., H. Y., E.C.L., D.K., J.K., and S.Y.L.

Competing interests

The authors declare no competing interests.

Additional information

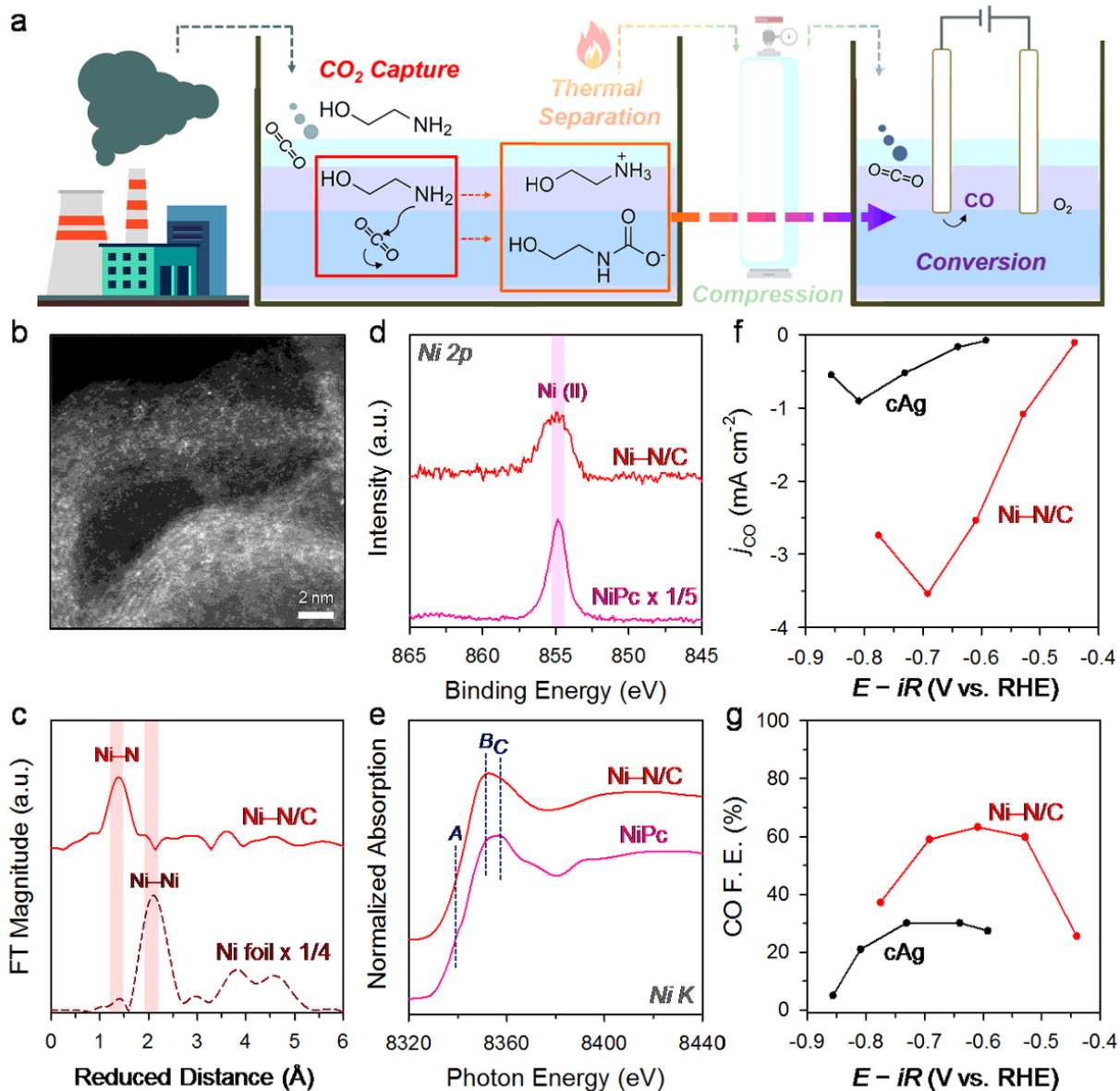**Correspondence and requests for materials** should be addressed to Yun Jeong Hwang.

Figures

Figure 1

Direct electroconversion of captured CO_2 with single atom Ni−N/C catalyst. a, Schematic illustration of direct electroconversion of captured CO_2. **b,** HAADF-STEM images of Ni−N/C. **c,** Ni K-edge k^3-weighted EXAFS spectra of Ni−N/C and Ni foil. **d,e,** Ni 2p XPS spectra (**d**) and Ni K-edge XANES spectra (**e**) of Ni−N/C and NiPc. **f,g,** j_{CO} (**f**) and CO F. E. (**g**) of Ni−N/C and cAg for the cCO$_2$RR in CO_2-adsorbed 5 M MEA solution.
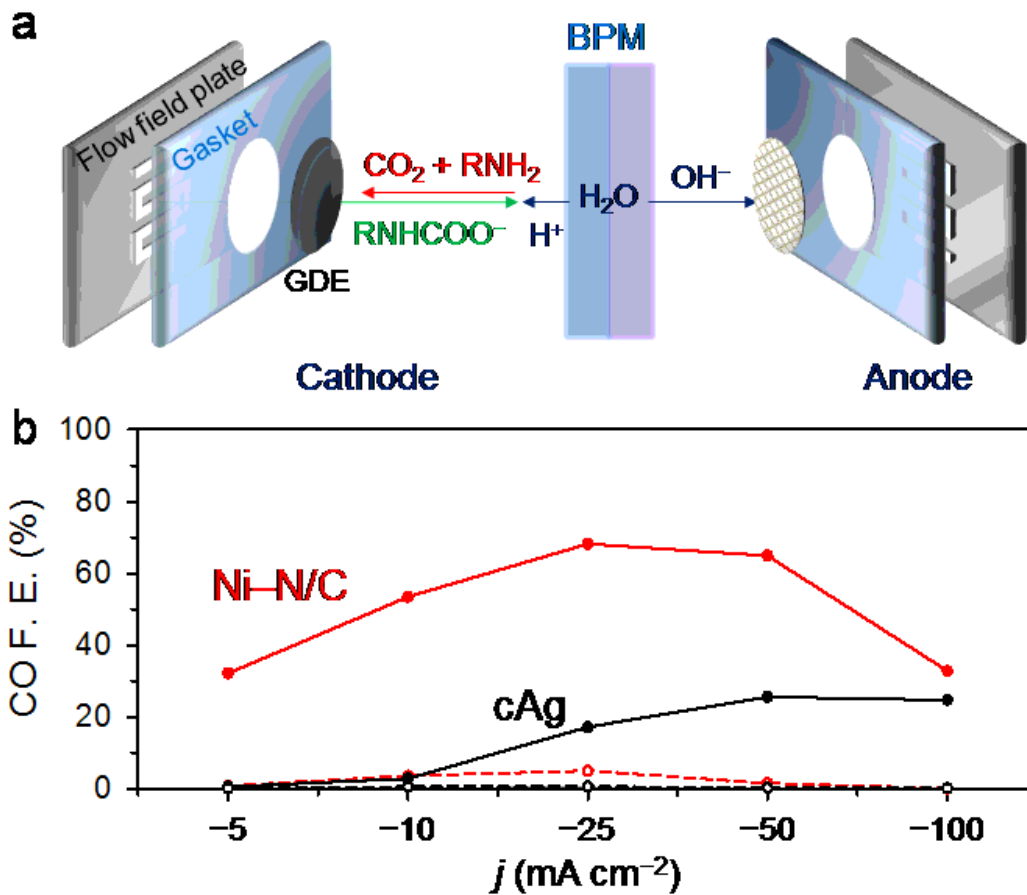
Figure 2

Membrane electrode assembly test for the cCO₂RR. a, Schematic illustration of CO_2 regeneration using BPM in the membrane electrode assembly. **b**, CO F. E. of Ni−N/C and cAg in chronopotentiometry using the membrane electrode assembly. The solid and dashed lines indicate the use of BPM and AEM, respectively.
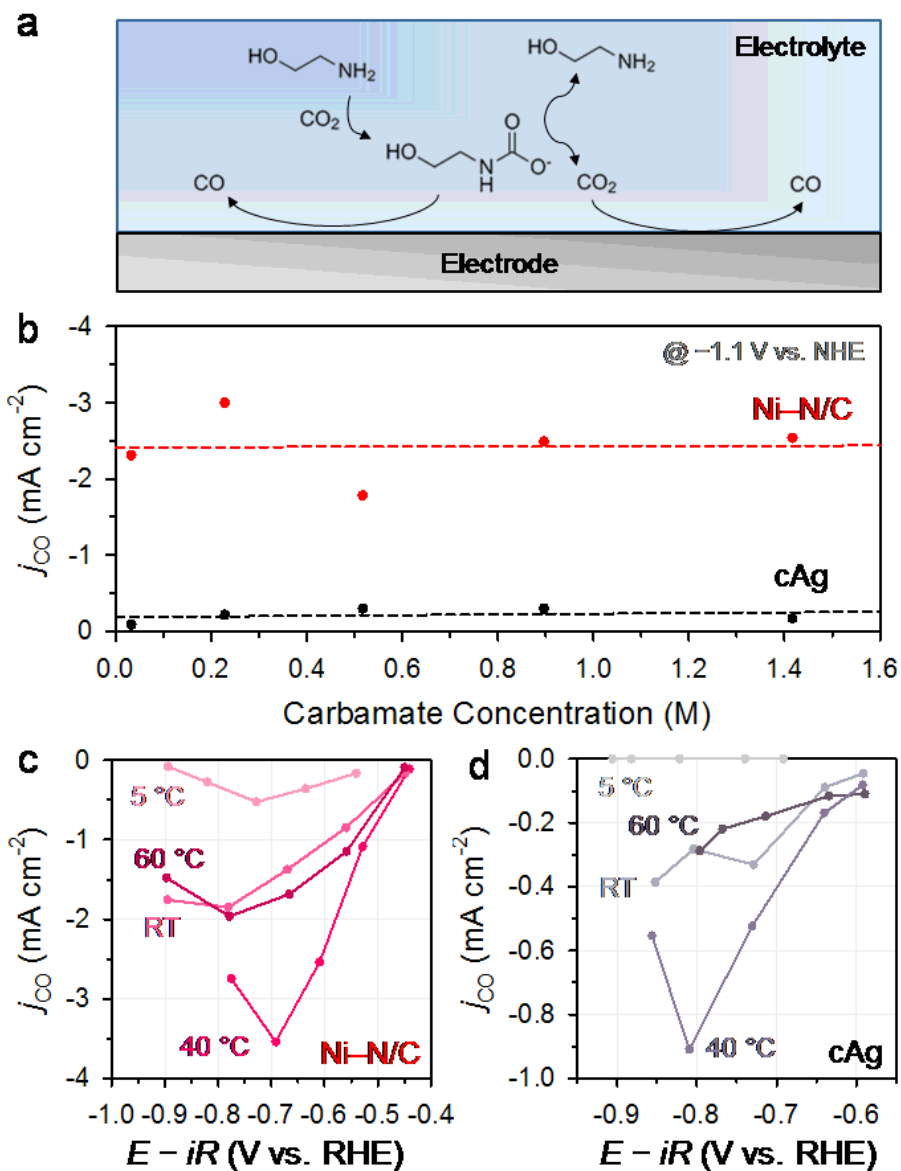
Figure 3

Investigation of the reaction pathway of cCO$_2$RR. a, Reaction pathways of two possible scenarios. **b**, j_{CO} at −1.1 V vs. normal hydrogen electrode (NHE) of Ni−N/C and cAg for the cCO$_2$RR in CO$_2$-adsorbed MEA (1−5 M) solutions with purging Ar. **c,d**, j_{CO} of Ni−N/C (**c**) and cAg (**d**) for the cCO$_2$RR in CO$_2$-adsorbed 5 M MEA in different temperatures.
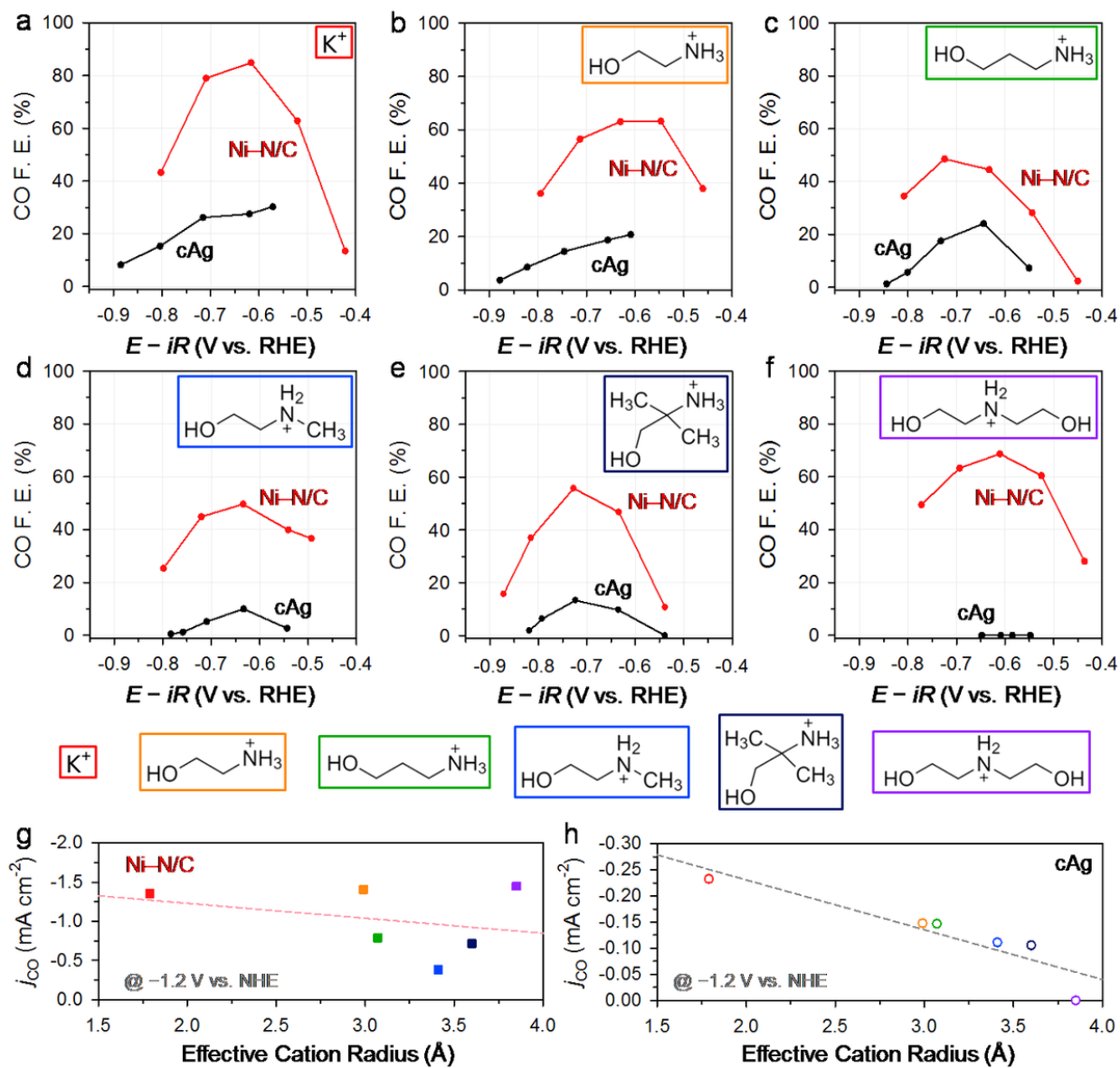
Figure 4

Universality of Ni−N/C in various capturing media for the cCO$_2$RR. a−f, CO F. E. of Ni−N/C and cAg for the cCO$_2$RR in CO$_2$-adsorbed 1 M KHCO$_3$ (**a**), 1 M MEA (**b**), 1 M 3-amino-1-propanol (**c**), 1 M 2-(methylamino)ethanol (**d**), 1 M 2-amino-2-methyl-1-propanol (**e**), and 1 M diethanolamine (**f**) solutions with purging Ar. **g,h**, j_{CO} of Ni−N/C (**g**) and cAg (**h**) with respect to effective cation radius at −1.2 V vs. NHE.
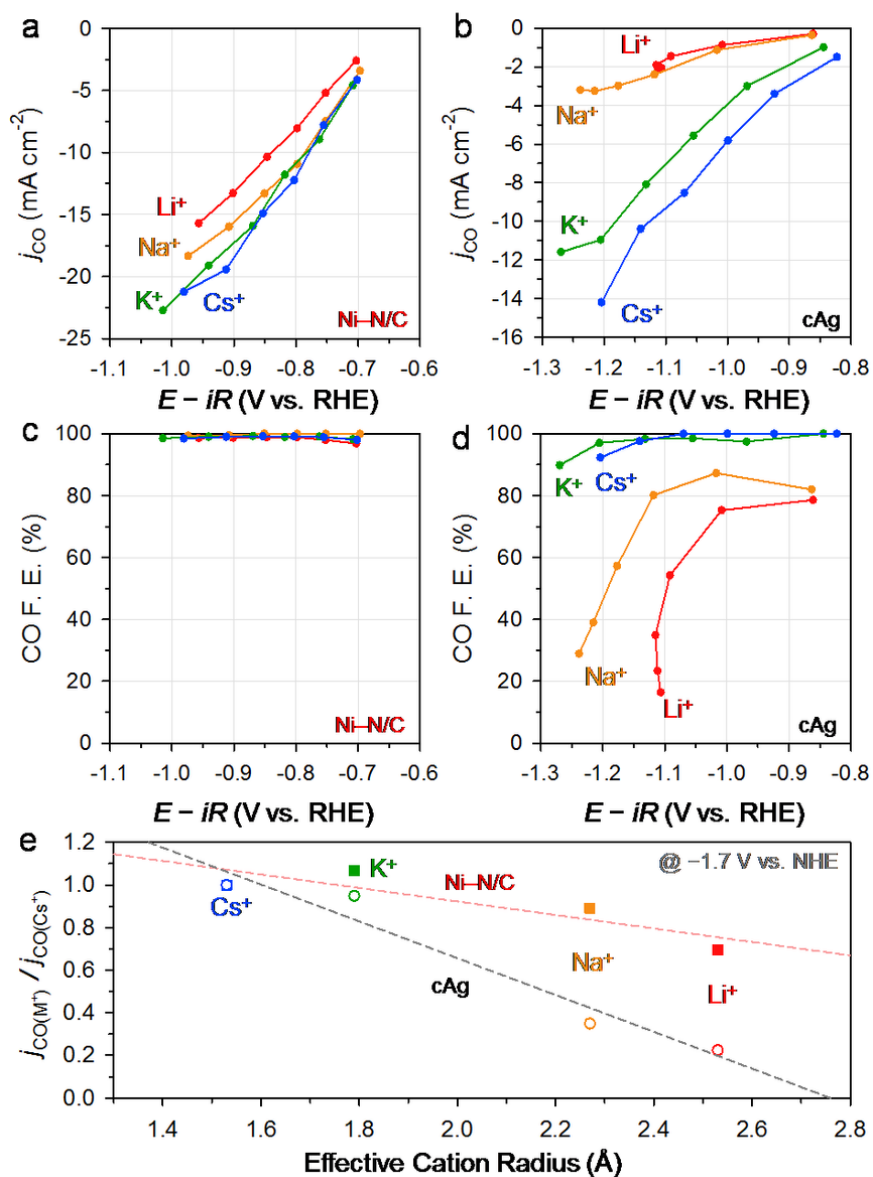
Figure 5

Cation effect and sensitivity of catalysts for conventional CO$_2$RR. a,b j_{CO} and **c,d** CO F. E. of Ni−N/C (**a,c**) and cAg (**b,d**) with the electrochemical CO$_2$RR in 0.05 M carbonate electrolytes containing different alkali metal cations. **e,** Normalized j_{CO} by j_{CO} in the presence of Cs$^+$ with respect to the effective cation radius at −1.7 V vs. NHE.

Supplementary Files

This is a list of supplementary files associated with this preprint. Click to download.

- Onlinefloatimage6.png
- 20220128CapturedCO2SISubmission.pdf